Quadratic phase modulation and diffraction-limited microfocusing generated by pairs of subwavelength dielectric scatterers

Azeddine Tellal, Omar Ziane, Safi Jradi, Olivier Stéphan, Patrice L. Baldeck

Research article

Azeddine Tellal, Omar Ziane, Safi Jradi, Olivier Stephan and Patrice L. Baldeck*

Quadratic phase modulation and diffraction-limited microfocusing generated by pairs of subwavelength dielectric scatterers

https://doi.org/10.1515/nanoph-2019-0071
Received March 3, 2019; revised April 14, 2019; accepted April 16, 2019

Abstract: Diffractive approaches are needed when refractive microlenses reach their focusing limit at the micron-scale in visible light. Previously, we have reported on micron-sized optical lenses based on the diffraction of metallic nanowires. Here, we extend our study to lenses based on pairs of subwavelength dielectric scatterers. Using simulations by two-dimensional finite element method, we demonstrate that focusing holds for pair spacings as small as the wavelength-size. For pairs with distances between inner walls larger than about 1.2λ, the scattered waves generate a quadratic phase modulation on the total propagating field leading to a diffraction-limited focusing i.e. an effective optical lens effect with high numerical aperture. In addition, they have low sidelobe intensities, long depths of focus, and they have a low sensitivity with polarization. For pairs with inner wall distances smaller than about 1.2λ, the focusing phase modulation is accumulated during the propagation through the dielectric pair structure. In this work, we report only on the experimental demonstration for the case of larger wall separation to emphasize on the scattered wave effect on micro-focusing. A pair of parallel polymer lines (cylindrical lens), and a grid of polymer lines (square microlens array) with 2 μm-spacing were fabricated by two-photon induced polymerization. Their focal lengths are comparable to their separating distances, their spot-sizes are 0.37 μm and 0.28 μm at wavelength 530 nm, and their focusing efficiencies are 70% and 60%, respectively.

Keywords: diffractive microlens; micron and sub-micron sizes; subwavelength dielectric scatterers; diffraction limited focusing; visible light.

1 Introduction

Flat optics based on metasurfaces is an emerging technology for the large scale diffusion of compact, lightweight, and cost-effective optical functions in high-tech products [1–3]. It is based on patterns of subwavelength structures that are designed (refractive index, size, geometry, orientation and arrangement) to obtain the amplitude and phase distributions needed for applications. To focus on, the main results have been the realization of ultrathin lightweight metalenses [4, 5] that have achromatic corrections [6, 7] and high numerical apertures [8–10] leading to low cost and easy to integrate lens components [11], weightless light concentrators [12] and miniature optical cameras [13].

Here, the challenge is the design of micron to submicron lenses that are needed to go with the constant shrinkage of pixel sizes in optical sensors i.e. 1.2 μm for current smartphone cameras and 0.8 μm for imaging sensors in development [14, 15]. As optical performances of refractive microlenses degrade for pixel sizes below 2 μm, alternative light collection strategies need to be investigated for submicron pixels [16, 17].

Metalens with a few micron sizes have been demonstrated with plasmonic [18, 19] and dielectric [20] subwavelength structures. However, their patterns need to have at least a few periods to generate the quadratic spatial phase modulation required for focusing. This is a hard limit for the design of submicron lenses in the visible spectrum.

***Corresponding author: Patrice L. Baldeck,** Université de Lyon, ENS de Lyon, CNRS UMR 5182, Université Claude Bernard Lyon 1, Laboratoire de Chimie, Lyon, France, e-mail: patrice.baldeck@ens-lyon.fr.
https://orcid.org/0000-0003-0979-0611
Azeddine Tellal and Omar Ziane: Laboratory of Quantum Electronics, Physics Faculty, University of Sciences and Technology – USTHB, Algiers, Algeria
Safi Jradi: Institut Charles Delaunay, CNRS UMR 6281, Université de Technologie de Troyes, Troyes, France
Olivier Stephan: Laboratoire interdisciplinaire de physique, CNRS UMR 5588, Université Grenoble Alpes, Grenoble, France

Alternative approaches can only be based on focusing effects that originate from a few structures. For example, single structures that have been designed to produce photonic nanojets can generate efficient focusing with structure sizes as small as 0.4 μm for a laser wavelength of 633 nm [21]. However, the focalized intensities are localized very near to their surfaces that limits the accessible depth for color filtering and photodiode detection.

A single structure with optical discontinuities can also lead to focusing based on the constructive interference of its diffracted waves. Diffraction focusing is a fundamental effect that occurs during the free evolution of a spatially limited wave packet [22–24]. Micro-slits in an obstructive material have shown diffraction-limited focusing, but they have large intrinsic blocking losses when organized in dense arrays [25, 26].

Previously, we have reported on using the diffraction of pairs of silver nanowires, with spacings of 1, 2 and 4 μm to obtain diffraction-limited focusing in the Fresnel region [27, 28]. Calculations based on the scalar Rayleigh-Sommerfeld integral highlighted the pure scalar diffractive contribution. This is a diffraction focusing scheme based on the spatial phase modulation generated by two scatterers.

In the present paper, we generalize our study to the case of dielectric scatterers that do not have the optical losses of metals. In the first part, we demonstrate by numerical analysis that, this type of focusing hold for pair spacings is as small as the wavelength-size. For spacings large enough, focusing arises from the two scattered waves that produce a quadratic phase modulation on the total field propagating below the pair. This is a general phenomenon that is little affected by their shapes and materials. It just needs enough scattered field amplitudes to obtain a significant interference contrast with the incident field. For smaller spacing sizes, down to the wavelength-size, focusing is maintained, but with a different physical origin. In this case, the spatial phase modulation is accumulated during the propagation through the dielectric pair. Our calculations point out its potential to be used with materials with low refractive index (i.e. $n = 1.4$) with micron-size structure heights. In the second part, we report on the experimental demonstration that corresponds to the case of larger wall distance. A cylindrical microlens, and a square microlens array based on polymer lines (width = 0.4 μm, height = 0.9 μm) spaced by 2 microns were fabricated by two-photon induced polymerization. The diffraction-limited focusing is demonstrated with focusing efficiency up to 70%.

2 Diffraction patterns for single and pair of rectangular dielectric scatterers (2D-FEM)

Numerical simulations were performed by using the two-dimensional finite element method via COMSOL multiphysics (radio-frequency module). Perfectly matched layers were set far from the objects to avoid reflections. The mesh size was set to be at least 10 elements per λ.

We study the diffraction pattern of rectangular structures that are the most convenient to fabricate on the large scale. For a single structure, the overall dimensions are chosen to maximize the scattered intensity. When increasing dimensions, the scattered pattern changes from a dipole emission pattern to more intense Mie scattering patterns at wavelength sizes. The dimensions are selected to obtain the most intense scattering while keeping a single lobe pattern, and to be compatible with the pair separation distances. Once the rectangle width is fixed, its height is optimized to obtain a destructive interference just below the structure for insuring low intensity sidelobes in the focusing pattern (SI. Figure 1).

In the following simulations, we have chosen, by simplicity, rectangular scatterers suspended in air having a width $W = \lambda$ and an optimized height $H = 2\lambda$. As described in SI. Figure 2, the maximum scattered power is obtained for $H = 1.5\lambda$, however the minimum transmitted power below the structure is obtained for $H = 2\lambda$. The refractive index of $n = 1.4$, typical of low-refractive index polymers, has been selected to test the limit of this focusing effect. Larger refractive indexes lead to smaller structures.

The scattered intensity pattern for an incident plane wave propagating along the z-axis with in-plan linear polarization is shown in Figure 1 (left). It is a forward scattering lobe with quasi-spherical wave fronts as shown in Figure 1 (right). The normalized forward scattered power is $P_{FSCAT} = 3.5$, i.e. calculated by the spatial integration of its normalized scattered intensity in $z > 0$ space. The total diffraction pattern results from the interference of this scattered radiation with the incident plane wave as shown in Figure 1 (middle). It consists of bright and dark trajectories that correspond to constructive and destructive interferences between the incident and scattered waves. The scattered field along the first trajectory has an amplitude with the same order of magnitude as the incident wave amplitude that leads to a good fringe contrast. As designed, the optimized rectangle height leads to a π–dephasing, and an efficient destructive interference below the structure.

When two diffractive structures are associated at the micron-scale, their scattered waves interfere with the

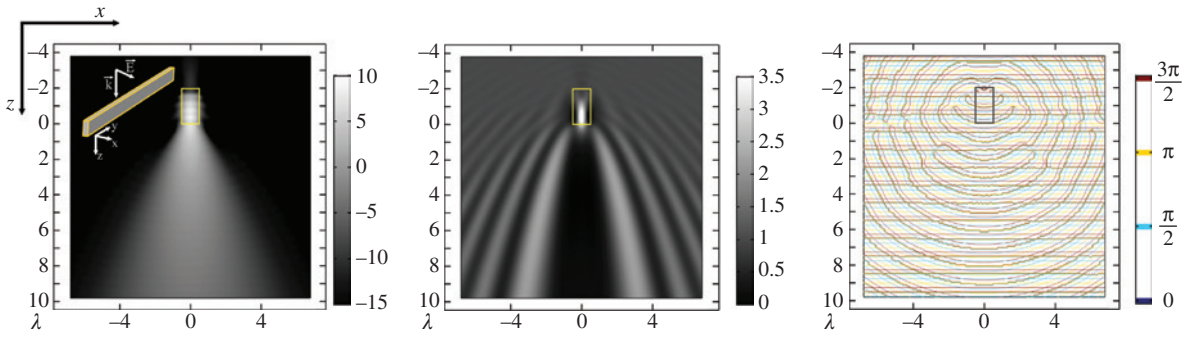

Figure 1: Calculated intensity patterns and phase map generated by a dielectric rectangular structure (W = λ, H = 2λ, n = 1.4) in air with an incident plane wave (in-plane polarization).
Left: scattered intensity pattern (logarithm scale). Middle: diffraction intensity pattern resulting from the interference of the scattered field with the incident field (linear scale). Right: phase maps of the scattered and incident fields. The spatial scales are normalized to λ.

incident plane wave, to form a microfocusing pattern with a diffraction-limited resolution [27, 28]. The scattered and total diffraction intensity patterns from pairs of dielectric rectangles with separating distance D = 4λ are shown in Figure 2. Focusing occurs at the focal length $Z_f = 3.9\lambda$ that leads to a numerical aperture NA = 0.54. The lateral resolution is $FWHM_x = 0.8\lambda$ that is a little smaller than the diffraction limited value 0.5/NA = 0.92λ. The depth of focus $FWHM_z = 5.2\lambda$ is larger than the diffracted limited $1/NA^2 = 3.27\lambda$. The maximum normalized intensity is $I_{max} = 4$, the normalized focused power (I_{max}*$FWHM_x$) is 3.36, and the focusing efficiency is η = 67%. The focusing efficiency is defined by the ratio between the focused power $P_f = I_{max}$*$FWHM_x$ and the power incident on the total lens width $P_i = I_0$*(D + W). In addition, they have very low sideband intensity, 5.6% of the maximum intensity in Figure 3C, and they are almost insensitive to the incident linear polarization (see Table 1, and in SI. Figure 3 and SI. Figure 4). The microfocusing characteristics are summarized in Table 1.

At focus (x = 0λ, z = 3.9λ), the normalized scattered electric field is $E_{x_{scat}}^{Pair} = 0.985$ i.e. the square root of the intensity shown in Figure 2. By definition, it interferes in phase with the incident field, and leads to a total normalized intensity $|E_{total}|^2 = (1 + 0.985)^2 = 3.94$ that is the same as the FEM calculated value.

Notice that these types of microfocusing patterns are not specific of dielectric rectangular structures. As shown in SI. Figure 5 and SI. Table 1, they are only slightly sensitive to the geometry (disk, triangle and rectangle), and to

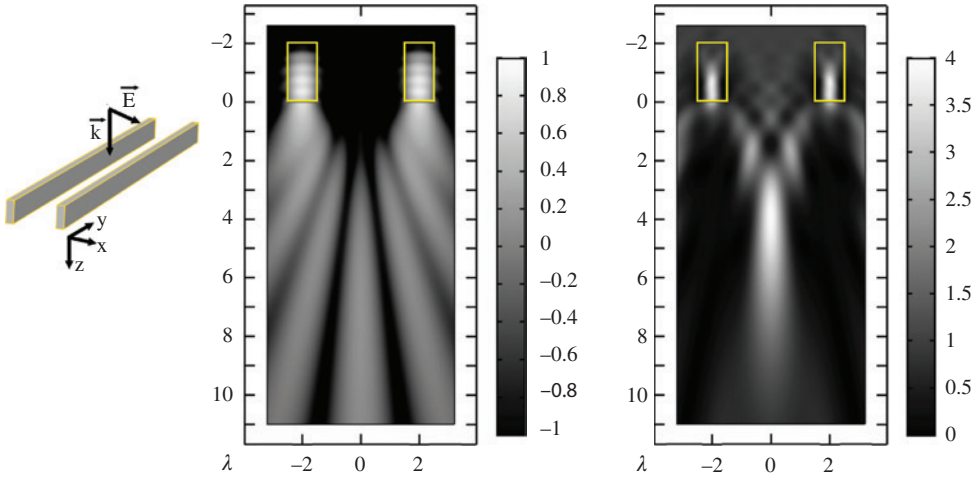

Figure 2: Calculated intensity patterns generated by a pair of dielectric rectangular structures (W = λ, H = 2λ, spacing D = 4λ, n = 1.4 in air with an incident plane wave (in-plane polarization).
Left: scattered intensity pattern (logarithm scale). Right: diffraction intensity pattern resulting from the interference of the scattered field with the incident field (linear scale). The spatial scales are normalized to λ.

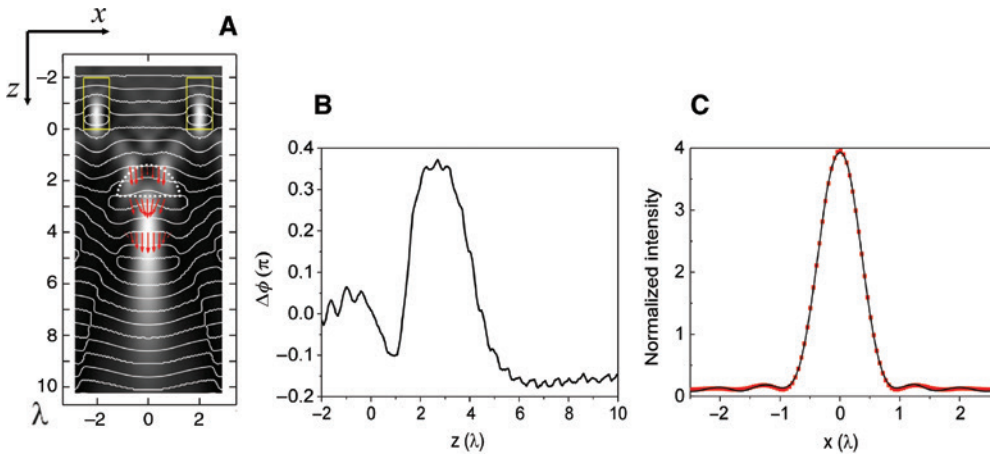

Figure 3: Optical characteristics of the "effective optical lens".
(A) Phase and intensity maps for a pair of rectangles (W = 2λ, H = λ, n = 1.4, D = 4λ). The red arrows represent the Poynting vectors at the entrance, the exit and the focal planes of the effective focal lens (represented by the dashed lens shape). (B) Phase accumulation on the focal axis (x = 0, z) generated by the effective lens. (C) Lateral intensity distribution (black) at focus (x, z = 3.9λ) compared with the diffraction limited Airy distribution with numerical aperture NA = 0.64 (red doted).

Table 1: Calculated optical characteristics of the microfocusing pattern.

Polarization	Focal length Z_f (λ)	FWHM$_x$ (λ)	FWHM$_z$ (λ)	$\frac{I_{max}}{I_0}$	η (%)	NA
In plane	3.9	0.80	5.25	3.94	63.4	0.54
Out of plane	4.1	0.87	5.84	3.56	61.6	0.52

Z_f, FWHM$_x$, FWHM$_z$, $\frac{I_{max}}{I_0}$, η and NA are respectively the focal length, the lateral resolution, the depth of focus, the normalized intensity at the focal point, the focusing efficiency, and the numerical aperture.

the material (dielectric or metallic) of scattering elements. Typically, microlens with separating distance D = 4λ have focal lengths $Z_f = 2.6\lambda - 3.9\lambda$, i.e. in the same order of magnitude of their separation distance (D = 4λ) leading to high numerical apertures in the NA = 0.54–0.69 range. Their focal spots have lateral resolution and depth of focus in the 0.7λ–0.8λ and 2.7λ–5.2λ ranges, respectively. They are 10%–20% smaller than diffraction-limited sizes predicted by their numerical apertures. They have low sidelobes, and are little sensitive to the incident polarization. Polymer microlenses have higher focusing efficiencies, up to 60%, that is ×4 more than silver for the same rectangular geometry.

The optical focusing properties do not change drastically with small increments of geometry parameters for dielectrics with low refractive indexes. For optimized geometries, typical increments of 5% in width or height lead to about 10% changes in optical characteristics. However, using materials with high refractive indexes leads to much smaller geometries, and tighter fabrication tolerances. For example, the optimized geometries for TiO_2 and Si are (W = 0.2λ, H = λ) and (W = 0.12λ, H = 0.72λ), respectively.

The focal lengths scale mainly with the separating distances of scatterers is shown by the intensity patterns in SI. Figure 6, and the characteristics list in SI. Table 2. However, the focusing properties degrade for long focal lengths, i.e. large separation distances between structures (SI. Figure 7). Their focusing characteristics are reported in SI. Figure 8. In particular, the intensity of the side lobes increases to 25% and 52% for separation distances of 10λ and 20λ, respectively.

In the following, we discuss the physical origin of this type of micro focusing in the case of scatterer pairs with distance between inner walls large enough to let the incident plane wave to propagate freely between them. We show that the two scattered waves generate a quadratic phase modulation on the total field leading to the diffraction-limited focusing i.e. they lead to an effective optical lens effect with a high effective numerical aperture (NA_{eff}).

The spatial phase distribution of the total propagating field diffracted by the previous pair with D = 4λ is shown in Figure 3A. In the first region below the structures ($0 < z < 1.3\lambda$), the phase delays introduced by the dielectric structures lead to a first zone of secondary focal points. At z = 1.3λ, the main focusing region begins with a plan of constant phase distribution between the structures for $-\lambda < x < \lambda$. Then, when the total field propagates, a quadratic phase modulation is accumulated with a maximum phase shift of 0.35 π. The latter occurs at z = 2.7λ between the lens axis (x = 0), and the locations x = − λ and x = λ for which the total field is in phase with the incident plane

wave (Figure 3B). At this location, the Poynting vector distribution, shown in Figure 3A, has a large range of wave vector angles (up to ≈40°). When propagating further than 2.7λ, the total field focalizes at z = 3.9λ, where the phase delay reduces to zero and the radius of curvature changes in sign.

Thus, we can consider that a micron-size pair of diffractive structures generates an "effective optical lens" of width 2λ that we have highlighted in Figure 3A. Its entrance and exit planes are z = 1.3λ ($\Delta\phi = 0$) and z = 2.7λ ($\Delta\phi = 0.35\pi$), respectively. Its focal length, defined as the distance between its exit plane and the focal plane is $Z_f = 1.2\lambda$ that gives an effective numerical aperture of NA = 0.64. The lateral intensity distribution at the focal point is shown in Figure 3C. It is in excellent agreement with the diffraction-limited Airy distribution having a numerical aperture $NA_{eff} = 0.64$ and $FWHM_x = 0.8\lambda$. Thus, this explains the apparent sub-diffraction resolutions that we obtain using the geometrical numerical apertures.

Then, we estimate the percentage of incident power that is localized in the focal region with this "effective optical lens". A normalized power of 5 is incident on the rectangle pair. Only an incident power of 2 propagates between the structures within the effective lens width ($-\lambda < x < \lambda$). Calculations show that the forward-scattered power by a single rectangle is 3.5. Half of it is scattered towards the focal region, and only a fraction in the focal region. The power scattered by the pair in the focal region is calculated to be 1.2 by integrating its scattered intensity pattern (Figure 2-left) in the effective lens region. Thus, there is a total power of 3.2 in the focal region that is 64% of the incident power, which is in good agreement with the FEM calculated value of 63.4%.

In the following, we investigate the effect of reducing separating distances in the sub-micron scale visible i.e. from 1 μm to 0.5 μm which is from 2λ to λ for the wavelength 0.5 μm. The rectangular width is set at W = 0.3 μm to fit with the smallest separating distance. The corresponding optimized height is H = 0.9 μm. For these calculations, we use the refractive index n = 1.52 of borosilicate glass to mimic the dielectric layer in between the microlens array and the photoactive layer in sensors. The incident plane wave is in-plane polarized. It interacts with scatterers in air before propagating further and focusing on the glass layer. The diffraction intensity patterns generated in the glass layer are displayed in Figure 4. Microfocusing patterns are obtained for all separating distances. One can distinguish two types of focusing behaviors.

For distances larger than about 1.2λ, we are in the case of pairs with inner wall separation distances large enough to let the incident plane wave to propagate freely between them, as we discussed above. The focusing region is determined by the location of constructive interferences between the incident plane wave and the scattered waves. For pairs with wall separation distances smaller than about 1.2λ, the free-space between the structures becomes too small to maintain an incident plane wave. The propagation is confined in the light guide structures before focusing in the free-space. The focusing occurs from a spatial phase modulation that is accumulated at z = 0 after

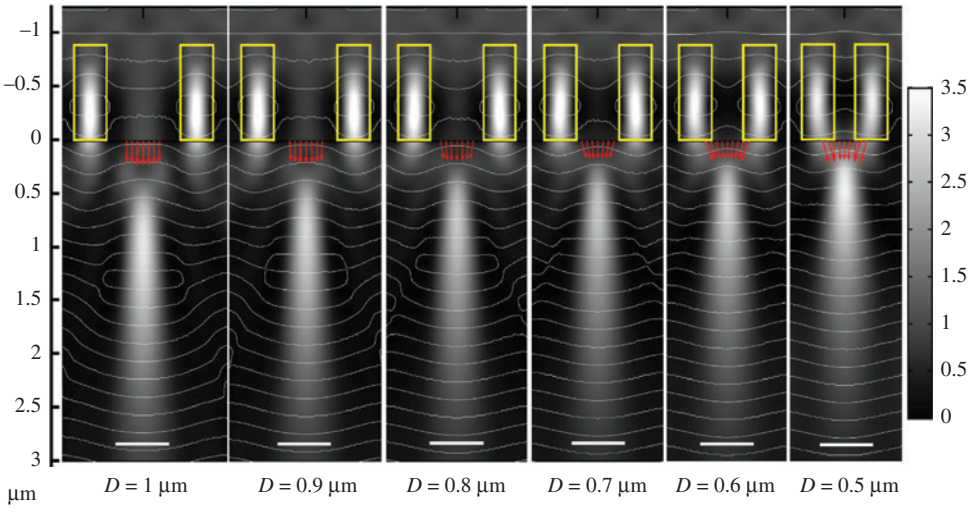

Figure 4: Diffraction intensity patterns generated by pairs of dielectric rectangles (W = 0.3 μm, H = 0.9 μm, n =1.52) for separating distances D = 1 μm, 0.9 μm, 0.8 μm, 0.7 μm, 0.6 μm, 0.5λ.
The scatterers are in air and focalization occurs in the dielectric (n = 1.52). The scale bar corresponds to a length 0.5 μm, i.e. it λ for the wavelength 0.5 μm.

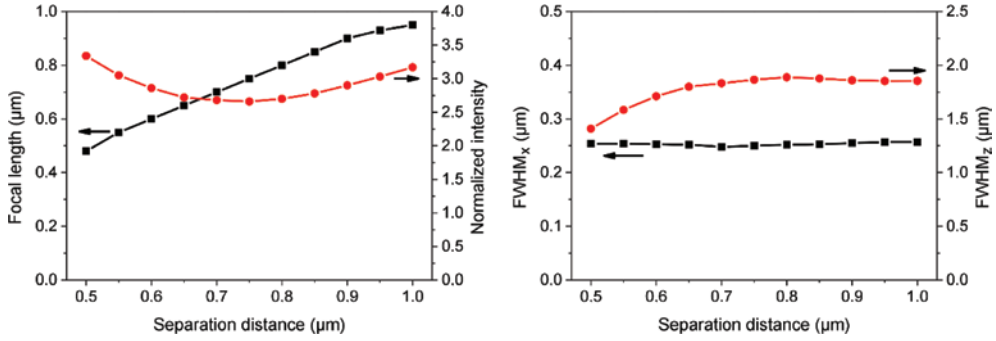

Figure 5: Evolution of optical characteristics with respect to the decrease of the separation distance below 1 μm.
Left: variations of focal lengths (black squares) and normalized maximum intensities (red circles) with the separation distance. Right: lateral resolution $FWHM_x$ (black squares) and depth of focus $FWHM_z$ (red circles) variations with the separating distance.

propagation in the dielectric pair. It does not originate from the scatter waves as in the case of pairs with larger separating distances.

The microfocusing characteristics of sub-micron lenses are summarized in Figure 5. The focal lengths are similar to the separation distances. The lateral resolutions and maximum intensities are almost constant with the values $FWHM_x \approx 0.255$ μm and $I_{max} \approx 2.8$. The depth of focus is about $FWHM_z \approx 1.8$ μm.

3 Experimental demonstration of a cylindrical lens (parallel polymer lines), and a square microlens array (grids of polymer lines) with 2 μm-spacing

In the following, we report on the fabrication and focusing properties of microlens based on parallel polymer microlines with a spacing of 2 μm. Microlines were fabricated by two-photon induced polymerization of pentaerythritol triacrylate ($n \approx 1.5$) on borosilicate cover glass ($n = 1.52$) using the method described previously [21]. Polymer lines were designed to have a length of 20 μm, and a nominal rectangular cross-section (width $W = 0.4$ μm and height $H = 0.9$ μm). Two types of microlens were fabricated- 1) cylindrical microlens based on pairs of parallel lines with 2 μm spacing and 2) arrays of square microlens based on grids of parallel lines with 2 μm spacing. In order to optimize the line dimensions, that are very sensitive to fabrication parameters, several groups of microlenses with different laser powers were fabricated. Optical characterization was done on "optimized geometries" that were distinguished by their most intense diffraction patterns and lowest intensity below the scatterers.

The experimental diffraction patterns were measured by 3D wide-field transmission imaging using an inverted microscope (Zeiss Axivert 200) with an oil immersion objective (Zeiss Plan Apochromat, ×100 NA = 1.4). The incident illumination, from a collimated non-polarized halogen white light, was spatially narrowed (diameter < 1 mm) to improve its spatial coherence. The 3D diffraction patterns were obtained by taking z-stacks of RGB images at different depths (0.1 μm-spacing) inside the glass substrate using a piezo scanner (PI Nanocube P-611), and CMOS camera Canon EOS-70D. The SI. Figure 9 shows the schematic of the characterization set up.

3D diffraction patterns were characterized inside the cover glass to obtain the best resolution by using an oil-immersion microscope objective. In order to compare experimental patterns with calculated FEM patterns, a further 3D deconvolution was applied on stack images using an open software package for 3D deconvolution [http://bigwww.epfl.ch/deconvolution/].

Similar results with focalization in air have been obtained with a dry objective (NA = 0.65), but with lower resolution (results not shown).

3.1 Cylindrical microlens based on diffractive polymer lines separated by 2 μm

The experimental white-light 3D diffraction pattern for a pair of parallel polymer lines separated by 2 μm is shown in Figure 6. The 3D intensity distributions from raw and deconvoluted Z-stack images are shown in Figure 6-left and Figure 6-right, respectively. The non-polarized incident light propagates downwards. Just above the substrate surface, one can distinguish the part of light that is guided inside the wavelength-scale polymer lines that are delimited by the yellow cross-sections. It does not propagate inside the substrate, because of the line geometry

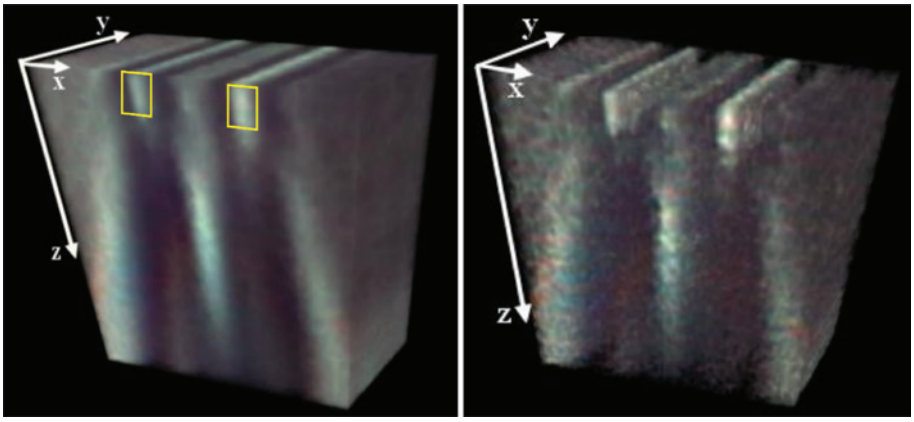

Figure 6: White-light 3D intensity distributions diffracted by a pair of parallel polymer lines separated by 2 μm.
Left: raw z-stack images. Right: deconvoluted z-stack images. Yellow rectangles represent line profiles (W = 0.4 μm and H = 0.9 μm).

(W = 0.4 μm and H = 0.9 μm) that has been designed to generate a π-dephasing with the surrounding light propagating in air. Thus, there is a dark shadow below the lines i.e. a destructive interference. As shown in Section 2, the two diffractive lines generate a quadratic phase modulation on the total field propagating below the structure. Thus, a clear focusing region is observed a few microns below the surface.

Figure 7 displays x–z projections of 2D-FEM, and experimental intensity distributions for red, green and blue colors. 2D-FEM intensity distributions are calculated inside the borosilicate substrate (n = 1.52) for the RGB color wavelength at 0.60 μm, 0.53 μm and 0.45 μm (Figure 7-1st row). Experimental intensity patterns are obtained by the RGB spectral decomposition of white light photographs before (Figure 7-2nd row), and after deconvolution (Figure 7-3rd row). All the experimental and calculated distributions show well-isolated focal regions below the diffractive lines. The longitudinal and the lateral intensity distributions in the focal axis (x = 0, z) and (x, Z_f) are displayed in Figure 8-1st and Figure 8-2nd rows, respectively. These plots were obtained from pattern images after the 3D deconvolution.

The corresponding data figures are reported in Table 2. The best correlation between experimental and calculated data are for the green wavelength for which the rectangular structure has been optimized (W = 0.4 μm and H = 0.9 μm) for a focusing in the glass substrate. The focal point is at 2.7 μm with resolutions $FWHM_x$ = 0.37 μm and $FWHM_z$ = 3.5 μm. The maximum focus intensity is about ×4.6 the incident intensity. The microlens has a collection efficiency of 0.71. These figures confirm that diffractive polymer lines are more efficient than metallic nanowires with similar geometry dimensions [27].

In Figure 8 and Table 2, one can notice that experimental focusing properties of red and blue colors differ significantly from simulations. This is due to large differences in spectral contents of calculated and experimental intensity distributions. Simulations are done with monochromatic waves (Red = 0.60 μm, Green = 0.53 μm and Blue = 0.45 μm), while the RGB optical channels of CMOS sensors are broad and overlapping. For our camera Canon EOS-70D, the red channel has a RGB content of (R = 0.51, G = 0.44, G = 0.05), the green channel (R = 0.08, G = 0.73, B = 0.19), and the blue channel (R = 0.03, G = 0.32, B = 0.65) [https://www.dxomark.com/Cameras/Canon/EOS-70D---Measurements]. Thus, red and blue channels have large green contents, which modify their focusing properties towards green channel properties.

Analysis of 2D-FEM characteristics of microlenses in Table 2 shows a large chromatic dispersion as RGB focal lengths are 2.0 μm, 2.6 μm and 3.6 μm, respectively. This should not be prejudicial for imaging sensor applications as the microlens have also large depths of focus that are compatible with the absorption depths of photodiodes.

3.2 Array of square microlenses based on grids of parallel lines with 2 μm spacing

The schematic of the polymer grid is shown in Figure 9-1st row. The 3D white light intensity distributions diffracted by the grid in borosilicate substrate are displayed in Figure 9-2st row (Left: z-stack of raw image data, Right: z-stack after 3D deconvolution). In comparison with cylindrical lens (Figure 6), grid intensities are more intense due to the double contribution of vertical and horizontal line pairs. In addition, there are several rows of focused light due to the interference of diffraction high-orders from neighbor

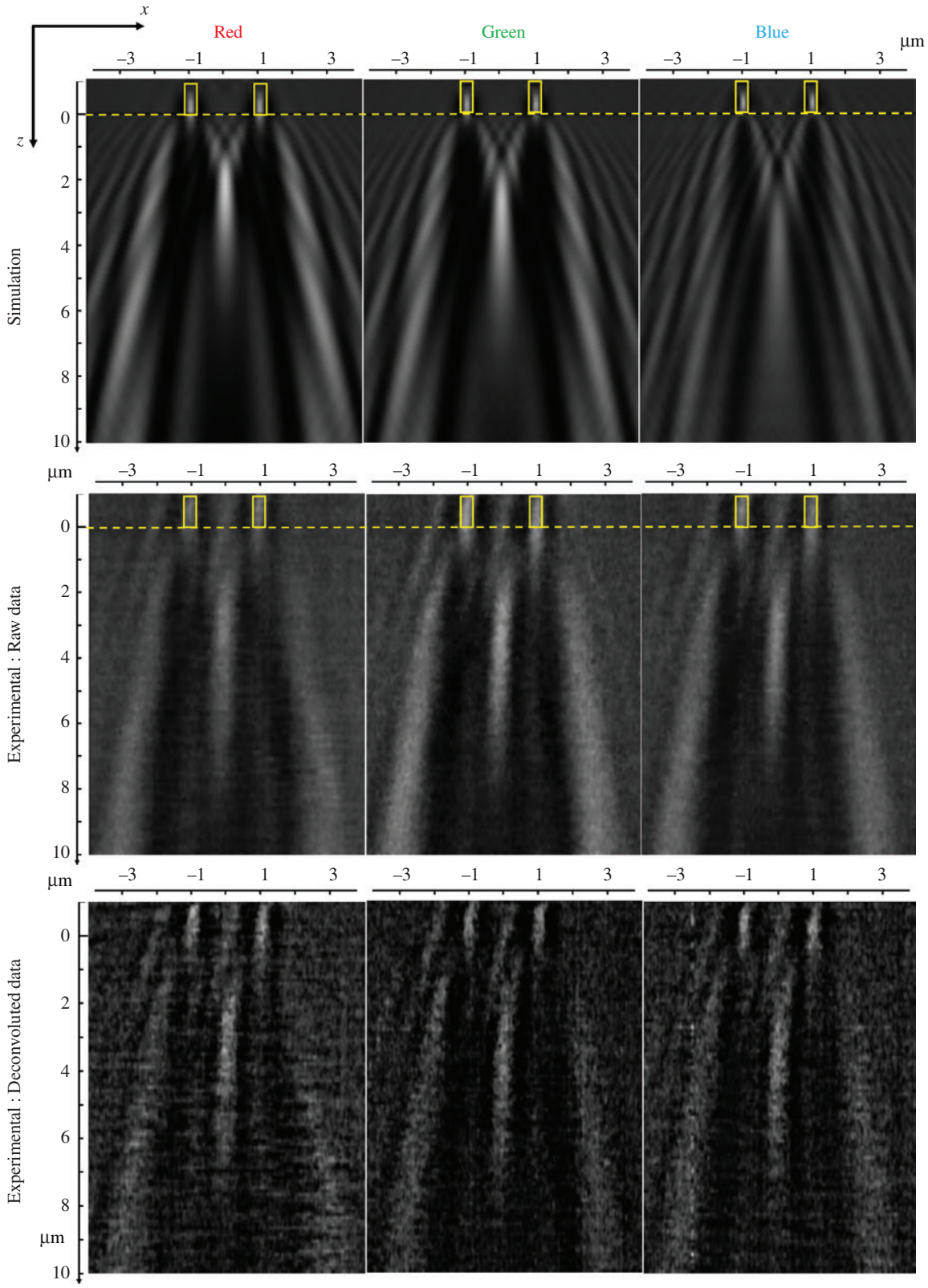

Figure 7: First row: 2D-FEM simulations of x–z diffraction intensity distributions by dielectric lines (width = 0.4 µm, height = 0.9 µm, n = 1.48) in a dielectric substrate (n = 1.52) for red (0.60 µm), green (0.53 µm), and blue (0.45 µm) wavelengths.
Second and third rows: experimental diffraction intensity distributions of polymer lines fabricated by two-photon polymerization on borosilicate substrate obtained from z-stack white light images, and after RGB color splitting.

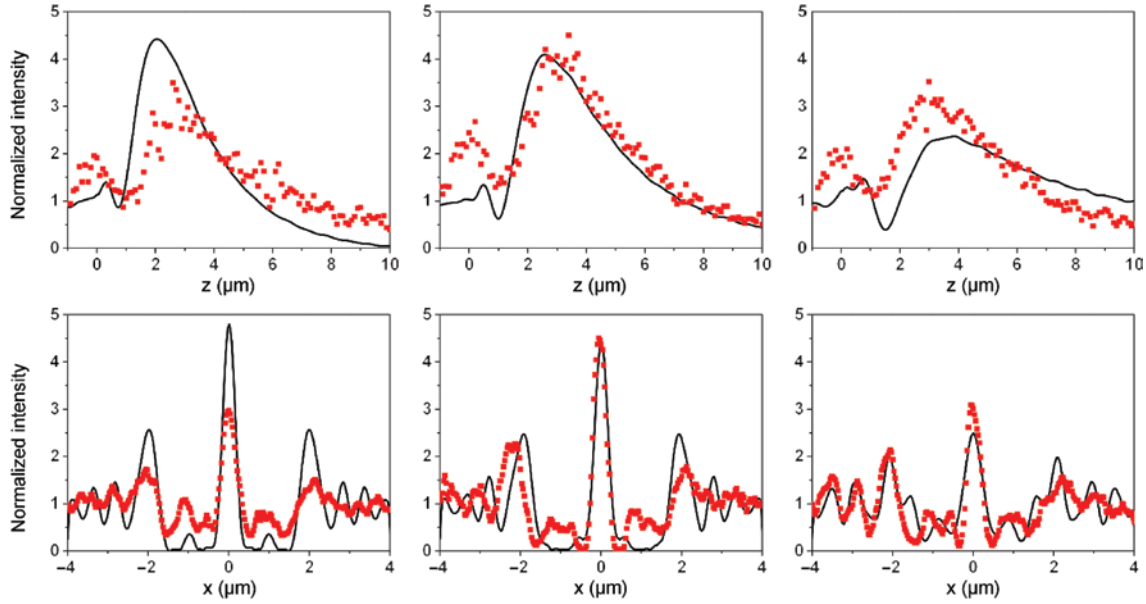

Figure 8: First and second rows: intensity distributions along the longitudinal focal axis (x = 0, z), and intensity distributions along the lateral focal axis (x, z = Z_f).
Solid lines for FEM simulations. Dotted lines for experimental data after deconvolution. Left, middle and right columns are for RGB color splitting, respectively.

Table 2: Optical characteristics of simulated (2D-FEM), and experimental cylindrical microlenses based on polymer parallel lines separated by 2 microns.

	Focal length (μm)	$FWHM_x$ (μm)	$FWHM_z$ (μm)	$\frac{I_{max}}{I_0}$	η (%)
Microlens D = 2 μm					
Simulation					
Red	2.0	0.35	2.8	4.8	70
Green	2.6	0.38	3.7	4.4	70
Blue	3.6	0.55	5.7	2.5	57
[a]	(2.0)	(0.33)	(1.8)	(2.2)	(32)
Experiment					
Red	2.8	0.45	3.5	3.0	56
Green	2.7	0.37	3.5	4.6	71
Blue	3.0	0.41	4.4	3.0	51
[a]	(1.9)	(0.32)	(1.14)	(2.2)	(31)

[a]Previous results obtained with silver nanowires for green [27].

square microlenses. In the x-z distributions, above the substrate level one can see the light that is guided inside the polymer lines, and the incident light that is propagating between them (Figure 9-3rd row: raw data, and Figure 9-4th row: deconvoluted data). As for the cylindrical lens, the guided light does not propagate in the substrate, leading to a dark shadow below the polymer lines. However, one can clearly see the propagation and focusing of the incident light located between the polymer lines.

The longitudinal and lateral intensity distributions along the focal axis are shown in SI. Figure 10. For green color, the focusing occurs at about 1.7 μm with resolutions $FWHM_x = 0.28$ μm, and $FWHM_z = 2.2$ μm. Its maximum normalized intensity is 8.4, and its collection efficiency is close to 60%. Using the diffraction-limited Airy function to analyze the lateral intensity distributions, the effective numerical apertures are 0.86, 0.94 and 0.88 for RGB colors, respectively. They are about 30% larger than for a single cylindrical lens, which is in agreement with 2D-FEM simulation of periodic cylindrical microlens. Thus, the effective lens induced by diffracted waves lead to an apparent superfocusing that does not break the diffraction-limited limit.

4 Conclusion

We report on the microfocusing that occurs with pairs of subwavelength dielectric scatterers. First, we demonstrate by 2D FEM simulations that it still occurs for pair spacings as small as the wavelength-size. For pair spacings large enough, the incident plane wave interferes with the scattered waves at focus. This is as if "an effective optical lens" is generated by the two scattered waves on the total propagating field. This new concept of "effective optical lens" rationalizes the calculated focusing efficiency, and

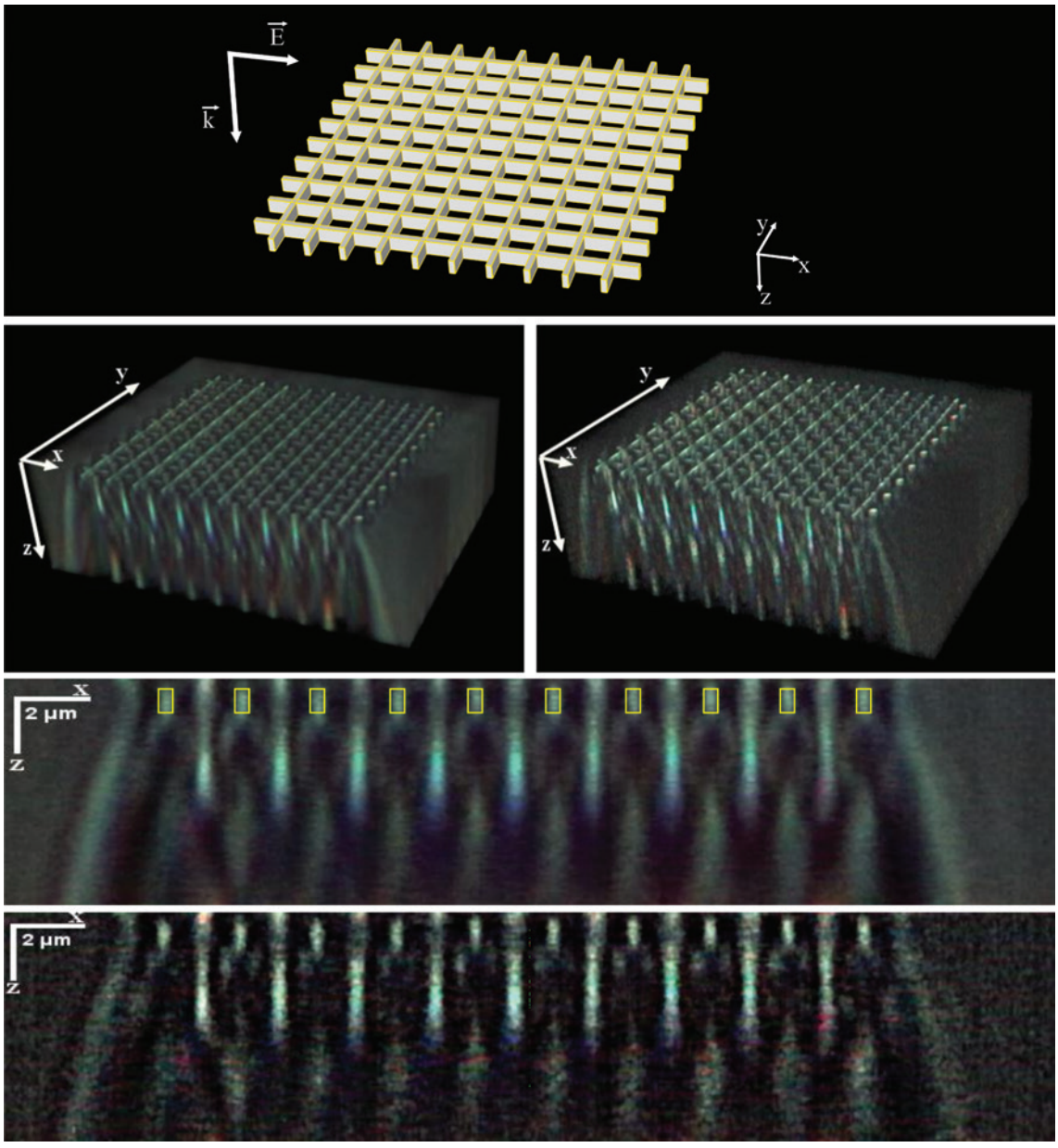

Figure 9: First row: The schematic of the polymer grid. Second row: white-light 3D intensity distributions diffracted by a grid of parallel polymer lines separated by 2 µm into a borosilicate substrate.
Left: raw z-stack images. Right: deconvoluted z-stack images. Third row: x–z projections of intensity distributions from raw data. Fourth row: x–z projections of intensity distributions from deconvoluted data.

the apparent superfocusing due to its effective numerical aperture that is a little larger than the geometrical numerical aperture. For pairs with smaller spacings, the spatial phase modulation is accumulated during the propagation through the dielectric pair structure.

Then, we present the experimental demonstration of a cylindrical lens and an array of square lenses based on parallel polymer lines with a separating distance of 2 µm. This corresponds to the case of larger wall distance to highlight the microfocusing effect generated by the scattered waves. Their focusing properties have been characterized by 3D wide-field transmission microscopic imaging with a non-polarized and partially-coherent white-light source. They have focal lengths comparable to their separating distance, whose spot sizes are 0.37 µm, and 0.28 µm. The resolution of periodic microlenses is significantly better than their unit-cell. This is confirmed by 2D-FEM simulations. In addition, their collection efficiencies are up to 70% for 1D cylindrical lens, and 60% for the array square unit.

Acknowledgments: The authors Pr. O. Ziane, and Dr. P.L. Baldeck thank Dr. G. Vitrant for visionary discussions in 2012 that lead to this research. Dr. P.L. Baldeck acknowledges the support for the project PHENOmenon. This project has received funding from the European's Union Horizon 2020 research and innovation programme under grant agreement n° 780278, Funder Id: http://dx.doi.org/10.13039/100010661. PHENOmenon project is an initiative of the Photonics Public-Private Partnership. Pr. O. Ziane and A. Tellal acknowledge the support from the France-Algeria PHC TASSILI 16MDU959.

References

[1] Kildishev AV, Boltasseva A, Shalaev VM. Planar photonics with metasurfaces. Science 2013;339:1232009.
[2] Yu N, Capasso F. Flat optics with designer metasurfaces. Nat Mater 2014;13:139.
[3] Lalanne P, Chavel P. Metalenses at visible wavelengths: past, present, perspectives. Laser Photonics Rev 2017;11:1600295.
[4] Aieta F, Genevet P, Kats MA, et al. Aberration-free ultrathin flat lenses and axicons at telecom wavelengths based on plasmonic metasurfaces. Nano Lett 2012;12:4932–6.
[5] Ni X, Ishii S, Kildishev AV, Shalaev VM. Ultra-thin, planar, Babinet-inverted plasmonic metalenses. Light-Sci Appl 2013;2:e72.
[6] Aieta F, Kats MA, Genevet P, Capasso F. Multiwavelength achromatic metasurfaces by dispersive phase compensation. Science 2015;347:1342–5.
[7] Wang S, Wu PC, Su V-C, et al. A broadband achromatic metalens in the visible. Nat Nanotechnol 2018;13:227.
[8] Arbabi A, Horie Y, Ball AJ, Bagheri M, Faraon A. Subwavelength-thick lenses with high numerical apertures and large efficiency based on high-contrast transmit arrays. Nat Commun 2015;6:7069.
[9] Khorasaninejad M, Chen WT, Devlin RC, Oh J, Zhu AY, Capasso F. Metalenses at visible wavelengths: diffraction-limited focusing and subwavelength resolution imaging. Science 2016;352:1190–4.
[10] Paniagua-Dominguez R, Yu YF, Khaidarov E, et al. A metalens with a near-unity numerical aperture. Nano Lett 2018;18:2124–32.
[11] Lin D, Fan P, Hasman E, Brongersma ML. Dielectric gradient metasurface optical elements. Science 2014;345:298–302.
[12] Moughames J, Jradi S, Chan T, et al. Wavelength-scale light concentrator made by direct 3D laser writing of polymer metamaterials. Sci Rep 2016;6:33627.
[13] Arbabi A, Arbabi E, Kamali SM, Horie Y, Han S, Faraon A. Miniature optical planar camera based on a wide-angle metasurface doublet corrected for monochromatic aberrations. Nat Commun 2016;7:13682.
[14] Takahashi S, Huang Y-M, Sze J-J, et al. A 45 nm stacked CMOS image sensor process technology for submicron pixel. Sensors 2017;17:2816.
[15] Li H, Micinski S, Dharia N, Boettiger U. Multi-color anti-reflection coating with silicon micro-lens photodiode for image sensor. In: Proc SPIE Optical Sensing, Imaging, and Photon Counting: From X-Rays to THz, San Diego, CA, USA, 2018;10729:5.
[16] Huo Y, Fesenmaier CC, Catrysse PB. Microlens performance limits in sub-2 μm pixel CMOS image sensors. Opt Express 2010;18:5861–72.
[17] Catrysse PB. Integration of optical functionality for image sensing through sub-wavelength geometry design. In: Proc SPIE Image Sensing Technologies: Materials, Devices, Systems, and Applications II, Baltimore, MD, USA, 2015;9481:8.
[18] Verslegers L, Catrysse PB, Yu Z, et al. Planar lenses based on nanoscale slit arrays in a metallic film. Nano Lett 2008;9:235–8.
[19] Yu Y, Zappe H. Effect of lens size on the focusing performance of plasmonic lenses and suggestions for the design. Opt Express 2011;19:9434–44.
[20] Özdemir A, Yılmaz N, Alboon SA, Takashima Y, Kurt H. Analysis of the focusing crosstalk effects of broadband all-dielectric planar metasurface microlens arrays for ultra-compact optical device applications. OSA Continuum 2018;1:506–20.
[21] Kotlyar VV, Stafeev SS, Feldman A. Photonic nanojets generated using square-profile microsteps. Appl Opt 2014;53:5322–9.
[22] Case W, Sadurni E, Schleich W. A diffractive mechanism of focusing. Opt Express 2012;20:27253–62.
[23] Weisman D, Fu S, Gonçalves M, et al. Diffractive focusing of waves in time and in space. Phys Rev Lett 2017;118:154301.
[24] Hu Y, Fu S, Li Z, Yin H, Zhou J, Chen Z. Focusing optical waves with a rotationally symmetric sharp-edge aperture. Opt Commun 2018;413:136–40.
[25] Vitrant G, Zaiba S, Vineeth BY, et al. Obstructive micro diffracting structures as an alternative to plasmonics nano slits for making efficient microlenses. Opt Express 2012;20:26542–7.
[26] Gonçalves MR, Case WB, Arie A, Schleich WP. Single-slit focusing and its representations. In: Exploring the World with the Laser: Dedicated to Theodor Hänsch on his 75th birthday. Meschede D, Udem T, Esslinger T, editors. Cham: Springer International Publishing, 2018:529–75.
[27] Zaiba S, Kouriba T, Ziane O, et al. Metallic nanowires can lead to wavelength-scale microlenses and microlens arrays. Opt Express 2012;20:15516–21.
[28] Ziane O, Zaiba S, Kouriba T, Bosson J, Vitrant G, Baldeck PL. Cylindrical planar microlens based on diffraction of parallel metallic nanowires. J Opt Soc Am B 2012;29:3277–85.

Supplementary Material: The online version of this article offers supplementary material (https://doi.org/10.1515/nanoph-2019-0071).